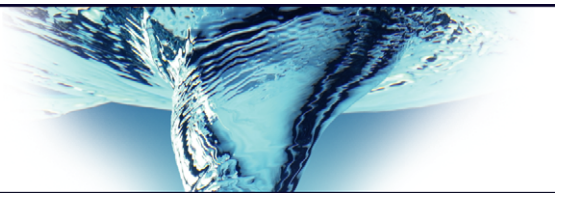
JFM RAPIDS
journals.cambridge.org/rapids



Energetics of horizontal convection

Bishakhdatta Gayen, Ross W. Griffiths†, Graham O. Hughes and Juan A. Saenz

Research School of Earth Sciences, Australian National University, Canberra, ACT 0200, Australia

(Received 14 August 2012; revised 15 October 2012; accepted 28 November 2012)

Three-dimensional direct numerical simulation of horizontal convection is reported for a large Rayleigh number, $Ra \sim O(10^{12})$, and boundary conditions that allow comparison with previous laboratory experiments. The convection is forced by heating over half of the horizontal base of a long channel and cooling over the other half of the base. The solutions are consistent with the experiments, including small-scale streamwise roll instability developing into a convectively mixed layer within the bottom thermal boundary layer, and a turbulent endwall plume. The mechanical energy budget is shown to be dominated by conversions of available potential energy to kinetic energy by buoyancy flux in the plume and the reverse in the interior of the circulation. These local conversions are three orders of magnitude greater than the total rate of viscous dissipation. The total irreversible mixing is exactly equal to the generation of available potential energy by buoyancy forcing, and one order of magnitude larger than the viscous dissipation. This confirms that dissipation rate is not an indicator of the strength of the circulation and explains why horizontal convection is more energetic than might be expected.

Key words: buoyancy-driven instability, convection, ocean circulation

1. Introduction

A number of experimental studies have shown that a gradient of temperature or heat flux along the horizontal boundary of a basin drives a convective circulation (referred to as horizontal convection) despite the constraint that, in a stationary state, there can be no net heat flux through the boundary or through any level in the fluid. Early experiments (Rossby 1965) (using a linear variation of temperature along the base of a box of length L and depth H, where $L = 2.5H$) with Rayleigh numbers (based on L) up to $Ra \sim 10^8$ gave a laminar circulation. Experiments in a larger box (using $L = 6.25H$ and a step difference on the boundary with either applied temperature or heat flux) (Mullarney, Griffiths & Hughes 2004; Stewart, Hughes & Griffiths 2011) achieved $Ra \sim 10^{12}$ and $Ra_F = 10^{14}$ ($Ra_F = Nu\,Ra$, where Ra_F is the Rayleigh number based on heat flux and Nu is the Nusselt number). These indicated that stability transitions occur at $Ra \sim 10^{10}$, leading to turbulence in the boundary layer and endwall

† Email address for correspondence: Ross.Griffiths@anu.edu.au

 © Cambridge University Press 2013
doi:10.1017/jfm.2012.592

https://doi.org/10.1017/jfm.2012.592 Published online by Cambridge University Press

plume at larger Rayleigh numbers. Experiments with salt flux and freshwater boundary conditions have achieved up to $Ra_F \sim 10^{19}$ (Stewart, Hughes & Griffiths 2012), and show an overturning circulation dominated by a turbulent plume.

The nature of the mechanical energy budget and how it relates to the magnitude of the mean flow, or to the role of instabilities and fluctuations, has not been fully explored (see Hughes & Griffiths 2008). An interesting result for the stationary state is obtained by horizontally averaging the kinetic energy equation (Paparella & Young 2002), leading to an expression for the volume-integrated rate of viscous dissipation $\varepsilon = g\kappa(\langle\rho\rangle_H - \langle\rho\rangle_0)WL$, where κ is the molecular diffusion coefficient for density, g the gravitational acceleration, the term in parentheses is the bottom-to-top difference in the horizontally averaged density and W is the width of the box. Thus dissipation vanishes in the limit of vanishing diffusivity, from which some authors have erroneously concluded that a strong convective flow cannot be maintained at very large (and geophysically relevant) Rayleigh numbers. However, the above expression for the dissipation rate is approximated by an upper bound that can be written as $\varepsilon \leqslant (\rho_0\kappa^3 W/L^2)Ra\,Pr/2$, where ρ_0 is the reference density, and dissipation increases with Ra (except in the case where Ra is increased by decreasing κ). Recent direct numerical simulations (Scotti & White 2011) corroborate the experiments and provide evidence that the flow is indeed turbulent according to several geometrical statistics, with heat being transported efficiently with small dissipation of kinetic energy. Progress has also been made in theoretical understanding of the generation of available potential energy (APE) by surface buoyancy fluxes and its conversion to kinetic energy (Hughes, Hogg & Griffiths 2009; Tailleux 2009), predicting that the total irreversible mixing rate must match the generation of APE. In the particular context of the ocean overturning circulation, analysis of solutions from general circulation models is providing evidence that the surface buoyancy forcing (convection) is important (and comparable to wind work) in driving the global circulation (Saenz *et al.* 2012). However, ocean circulation models involve energy from sources other than buoyancy, and subgrid parametrizations of unresolved flow (including diffusion, mixing and 'convective adjustment' schemes) that do not faithfully represent the energy budget.

Previous horizontal convection solutions include a two-dimensional model for large Ra (Mullarney *et al.* 2004) that compares well with the corresponding laboratory experiments in the same study, recognising that the boundary layer instability was constrained to two dimensions. Two-dimensional solutions at much smaller Ra gave steady flow for an endwall plume (and linear bottom temperature) (Rossby 1998) or an eddying flow for a central plume (and sinusoidal temperature) (Paparella & Young 2002). Recent three-dimensional direct numerical simulation (DNS) at Rayleigh numbers up to $Ra = 8\times10^{10}$ (based on half the box length for a central plume) showed circulation patterns consistent with the laboratory experiments, along with remarkably high energy efficiencies (Scotti & White 2011). However, only total box-integrated quantities were considered and important aspects of the physics in different regions of the flow were overlooked. The largest Ra studied is also close to that for onset of boundary layer instabilities (and the sinusoidal boundary condition is likely to shift onset to larger Ra or to a smaller fraction of the box length), whereas we will show here that almost all of the irreversible mixing at larger Rayleigh number occurs in the unstable boundary layer.

Here we present DNS results at a larger Rayleigh number than previously reported, comparing with the experiments of Mullarney *et al.* (2004) and Stewart *et al.* (2011). We present a new analysis of the energy budget, thereby confirming concepts

https://doi.org/10.1017/jfm.2012.592 Published online by Cambridge University Press

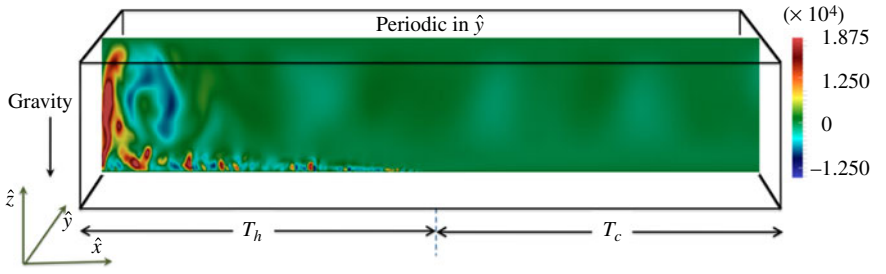


FIGURE 1. Schematic of the domain used for the applied ΔT case: the hot plate temperature is T_h ($\hat{T} = 1$) on the left half of the base ($0 \leqslant \hat{x} < 1/2$) and the cold plate temperature is T_c ($\hat{T} = 0$) on the right half of the base ($1/2 < \hat{x} \leqslant 1$). Superposed is a snapshot of the vertical velocity field $\hat{w}$ in the $\hat{x}$–$\hat{z}$ plane from the thermally equilibrated simulation.

previously discussed theoretically and explaining why the convection is energetic and partly turbulent. In order to illustrate the concepts, we focus in §§ 2 and 3 on a given Ra with applied temperature difference, backed up by a run with applied flux. In order to further explain the energy balance, we develop a scaling theory in § 4.

2. Formulation of the problem

We examine convection in a channel of length L, height H and width W (in which direction the domain is periodic). For clarity we focus mainly on the case of imposed constant and uniform temperatures T_h and T_c over two halves of the base, as shown in figure 1. A second case was run with the same uniform T_c but a constant and uniform heat flux applied over the heating half of the base providing the same total heat throughput. All other boundaries are insulating. The fluid is assumed linear and Boussinesq, with kinematic viscosity ν, thermal diffusivity κ and coefficient of thermal expansion α. DNS is used to solve the dimensionless continuity, momentum and temperature equations:

$$\boldsymbol{\nabla}\cdot\hat{\boldsymbol{u}} = 0, \quad \frac{\mathrm{D}\hat{\boldsymbol{u}}}{\mathrm{D}\hat{t}} = -\boldsymbol{\nabla}\hat{p} + Pr\nabla^2\hat{\boldsymbol{u}} + Ra\,Pr\,\hat{T}\boldsymbol{k}, \quad \frac{\mathrm{D}\hat{T}}{\mathrm{D}\hat{t}} = \nabla^2\hat{T}, \tag{2.1}$$

where the dimensionless quantities (denoted by a hat) are the velocity $\hat{\boldsymbol{u}} = (\hat{u}, \hat{v}, \hat{w})$, the temperature deviation $\hat{T}$ from a reference value (T_c), the deviation $\hat{p}$ from the background hydrostatic pressure and time $\hat{t}$. The governing parameters are the Rayleigh number, Prandtl number and aspect ratio,

$$Ra \equiv \frac{\alpha g(T_h - T_c)L^3}{\nu\kappa} \quad \left(Ra_F \equiv \frac{\alpha g F L^4}{\rho_0 c_p \nu \kappa^2}\right), \quad Pr \equiv \frac{\nu}{\kappa}, \quad A \equiv \frac{H}{L}, \tag{2.2}$$

respectively, and dimensionless quantities are obtained using the scales for mass, length, time and temperature difference (relative to T_c): $\rho_0 L^3$, L, L^2/κ and $\Delta T = T_h - T_c$ (or $T_h|_{max} - T_c$), respectively. The simulations are conducted for $Ra = 5.86 \times 10^{11}$ (or $Ra_F = 6.41 \times 10^{13}$), $Pr = 5$ and $A = 0.16$. No-slip boundary conditions are used on the top, base and endwalls. Thus conditions correspond closely to those in the laboratory experiments of Mullarney *et al.* (2004) and Stewart *et al.* (2011):

https://doi.org/10.1017/jfm.2012.592 Published online by Cambridge University Press

$L = 1.25$ m and $H = 0.2$ m, imposed cooling temperature $T_c \approx 10\,^{\circ}$C and heating temperature $T_h \approx 40\,^{\circ}$C (or $F = 1154$ W m^{-2}), and water as the fluid.

The simulations use a mixed spectral/finite difference algorithm. Periodicity is imposed in the spanwise, $\hat{y}$ direction (of width $W = 0.04L$, which covers several convective rolls in the boundary layers) and derivatives are evaluated with a pseudo-spectral method. The grid is staggered in the vertical and streamwise directions, and the corresponding derivatives are computed with second-order finite differences. A low-storage third-order Runge–Kutta–Wray method is used for time stepping, except for the viscous terms, which are treated implicitly with the alternating direction implicit method. The computational grid has $513 \times 128 \times 257$ points in the $\hat{x}$, $\hat{y}$ and $\hat{z}$ directions, respectively, and is non-uniform in $\hat{x}$ and $\hat{z}$. The grid resolution $\Delta_{x,y,z}$ was compared with the Batchelor microscale, $\eta_b \sim (Pr)^{-1/2}\,(\nu^3/\varepsilon)^{1/4}$, and satisfied the criterion $[\Delta_x, \Delta_y, \Delta_z]_{max}/\eta_b \leqslant \pi$ proposed by Stevens, Verzicco & Lohse (2010). The strongest test of adequate resolution is the result that the energy budget (reported below) closed exactly.

The simulation with applied ΔT was initialized with an isothermal ($\hat{T} = 0.83$) tank of water that was motionless, but with a small amount of white noise concentrated near the bottom boundary. Thermal equilibration of the flow to a stationary state was monitored using time series of average temperature in the tank and the net heat transport through the base; equilibrium was judged to be reached after a time $\hat{t} = 3.7 \times 10^{-3}$ (with mean top temperature $\hat{T} = 0.952$), when no further secular change in these quantities is detected. The net heat input continued to fluctuate about zero with an amplitude of the order of 2 % of the heat throughput. The same equilibrium state was also approached from the opposite direction, beginning with established horizontal convection at an initial larger ΔT. The results discussed here represent the flow during a subsequent period $3.7 \times 10^{-3} < \hat{t} < 5.5 \times 10^{-3}$ (corresponding to 8–12 h in the experiments). The applied flux simulation was initiated with the applied ΔT equilibrium solution.

3. Simulation results

The flow field is similar to that observed in the corresponding experiments (Mullarney *et al.* 2004; Stewart *et al.* 2011). The temporally averaged velocity and temperature fields (figure 2) show a strongly asymmetric overturning. A stably stratified boundary layer on the base feeds into an unsteady plume against the endwall. The rising plume is cooled by entrainment of water from the interior, and subsequently enters the interior, largely against the upper boundary. The mean circulation is closed by a remarkably uniform downwelling towards the base, although internal gravity waves and large eddy-like motions are evident in the interior (figure 2*b*). The magnitude of these fluctuations decreases with distance from the plume. The interior is weakly stratified.

Details of the boundary layer structure are shown in figure 3. The stable thermocline is maintained by the basal cooling and drawn horizontally towards the plume. Convection above the heated region erodes the stable temperature gradient from below. Streamwise rolls (shown by the iso-surfaces of counter-rotating streamwise vortices $\widehat{\Omega}_x = [\nabla \times \hat{\boldsymbol{u}}] \cdot \boldsymbol{i}$) form at $\hat{x} \sim 0.44$, near the transition between the cooled and heated region of the base, and impact on the temperature field, as also shown by the spanwise corrugations in the surface $\hat{T} = 0.67$. Rolls remain coherent over a downstream distance $\sim$0.06–0.08. Interaction and merging of the coherent rolls is apparent

https://doi.org/10.1017/jfm.2012.592 Published online by Cambridge University Press

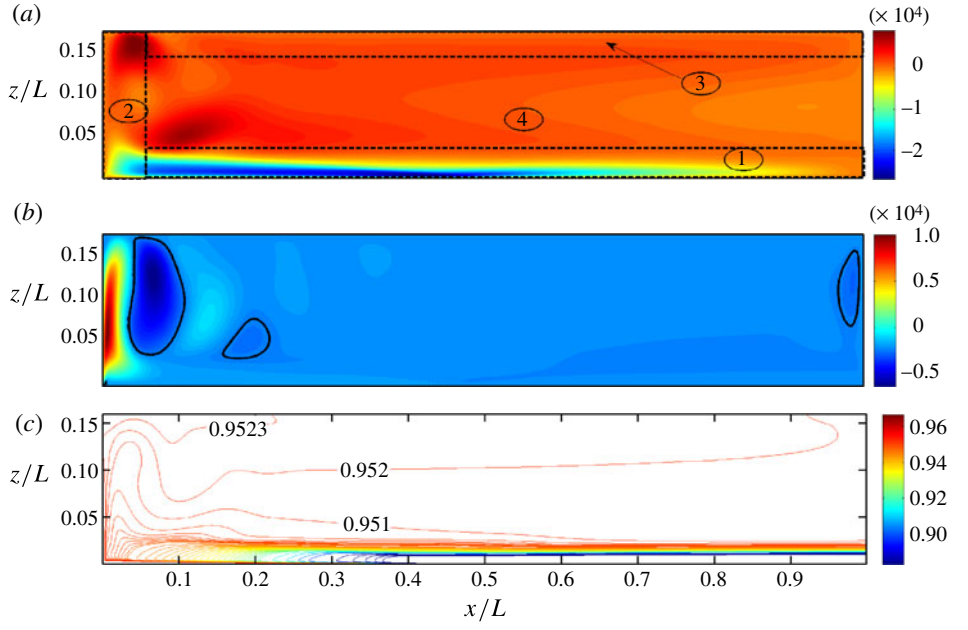


FIGURE 2. Time-averaged fields after thermal equilibration: (*a*) streamwise velocity, $\hat{u}$; (*b*) vertical velocity, $\hat{w}$; and (*c*) temperature, $\hat{T}$. The $\hat{w} = -625$ contour is shown in (*b*) as a black line. The channel has been divided into four different rectangular regions for subsequent analysis, as shown in (*a*): (1) lower boundary layer (LBL), (2) plume region, (3) upper boundary region (UBL) and (4) interior. See supplementary movies for views of the unsteadiness in the flow.

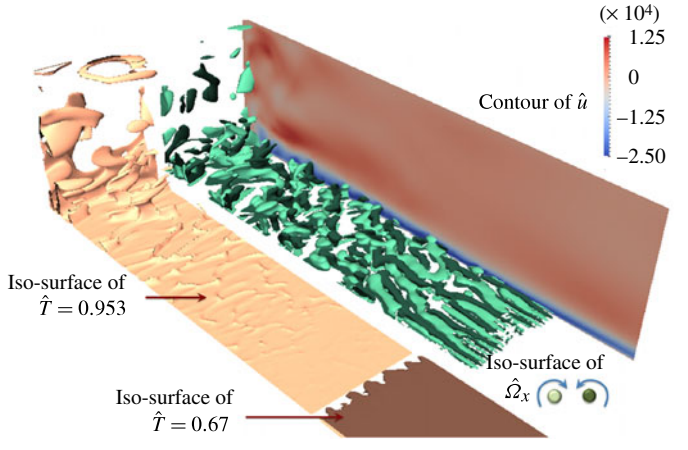


FIGURE 3. A three-dimensional snapshot of the thermally equilibrated flow. The vertical slice shows the contours of the streamwise velocity. Iso-surfaces ($\pm 2.3 \times 10^6$) of streamwise vorticity, $\hat{\Omega}_x$, and temperature are shown in the middle and front panels, respectively. The mean interior temperature is 0.952. See supplementary movies.

https://doi.org/10.1017/jfm.2012.592 Published online by Cambridge University Press

approximately one-third of the distance along the heated base, resulting in complicated three-dimensional structures. Mushroom-shaped plumes, inclined slightly leftward in the large-scale flow, dominate the convective mixed layer (see supplementary movies, available at http://dx.doi.org/10.1017/jfm.2012.592) and, as illustrated by the $\hat{T} = 0.953$ iso-surface, are less restricted by the overlying stratification as the flow approaches the left-hand endwall. At the endwall the stable gradient has been eroded and the convective elements maintain a turbulent plume through the full depth of the channel. All this behaviour is similar to that observed in the experiments (Mullarney *et al.* 2004).

Following Winters *et al.* (1995) and Hughes *et al.* (2009) we define (in dimensional terms), for a fluid volume V, the mean kinetic energy, $\overline{E}_k = \rho_0/2 \int \overline{u}_i \overline{u}_i \, \mathrm{d}V$, the turbulent kinetic energy, $E'_k = \rho_0/2 \int \overline{u'_i u'_i} \, \mathrm{d}V$, the potential energy, $E_p = g \int z\rho \, \mathrm{d}V$, the background potential energy, $E_b = g \int z_* \rho \, \mathrm{d}V$ and the available potential energy (APE), $E_a = E_p - E_b$. The mean (overbar) and fluctuating (primed) velocity components are evaluated in the spanwise $\hat{y}$ direction, u_i is the velocity in the ith direction and $z_* = z_*(\rho)$ is the height at which a parcel of density ρ would reside if the entire density field were allowed to relax adiabatically to equilibrium (termed the background state). The energetics framework derived by Hughes *et al.* (2009) relates these energy reservoirs and the rates of conversion between reservoirs, as shown schematically in figure 4.

For convection with no applied mechanical forcing ($\overline{\Phi}_\tau = \Phi'_\tau = 0$) and in the time-averaged thermal equilibrium ($\Phi_{b1} = 0$), the only non-zero forcing term in figure 4 is $\Phi_{b2} = g\kappa \oint z_*(\partial\rho/\partial x_j) n_j \, \mathrm{d}S$, where S is the surface bounding the volume. The remaining conversion rate terms are defined as follows: $\Phi_T = -\rho_0 \int (\partial \bar{u}_i/\partial x_j) \overline{u'_i u'_j} \, \mathrm{d}V$, $\overline{\Phi}_z = g \int \bar{\rho} \bar{w} \, \mathrm{d}V$, $\Phi'_z = g \int \overline{\rho' w'} \, \mathrm{d}V$, $\overline{\varepsilon} = \rho_0 \nu \int (\partial \overline{u}_i/\partial x_j)^2 \, \mathrm{d}V$, $\varepsilon' = \rho_0 \nu \int \overline{(\partial u'_i/\partial x_j)^2} \, \mathrm{d}V$, $\Phi_d = -g\kappa \int (dz_*/d\rho)(\partial\rho/\partial x_j)^2 \, \mathrm{d}V$ and $\Phi_i = -g\kappa WL(\langle\rho\rangle_H - \langle\rho\rangle_0)$, where $\langle\,\rangle_z$ denotes a horizontal area average at height z. These terms are evaluated from our simulations and time-averaged. The box-integrated values (normalized by Φ_i) are shown in figure 4.

The DNS confirms that the APE budget is dominated by an exact balance between the rate of energy supply by the surface buoyancy fluxes and the rate of dissipation due to irreversible mixing, i.e. $\Phi_{b2} = \Phi_d$, as predicted by Hughes *et al.* (2009) and Tailleux (2009). Mean and turbulent kinetic energy (KE) in the flow are supplied from APE at comparable rates $-\overline{\Phi}_z$ and $-\Phi'_z$, respectively, which in turn are in approximate balance with the corresponding viscous dissipation rate from each reservoir. Furthermore, the total dissipation $\overline{\varepsilon} + \varepsilon'$ is equal to both Φ_i (as predicted by Paparella & Young 2002) and the overall conversion of APE to KE via the net buoyancy flux $-\overline{\Phi}_z - \Phi'_z$ (as confirmed by Scotti & White 2011). The energy conversion rates fluctuate by 5 % about the time-averaged values. As a measure of the level of turbulence, velocity fluctuations account for approximately 40 % of the KE production and 60 % of the viscous dissipation.

The results show how the convection can be highly energetic while satisfying the bound on dissipation rate. Table 1 gives the normalized contributions to the mean flow buoyancy flux $\overline{\Phi}_z/\Phi_i$ from the regions of the flow shown in figure 2(*a*). It is apparent that integrating over the whole volume obscures physically important APE to KE conversions (as previously shown in an ocean general circulation model (Gregory & Tailleux 2011)). In particular, comparable and oppositely-signed rates of APE to KE conversion in the plume and interior regions are three orders of magnitude greater than

https://doi.org/10.1017/jfm.2012.592 Published online by Cambridge University Press

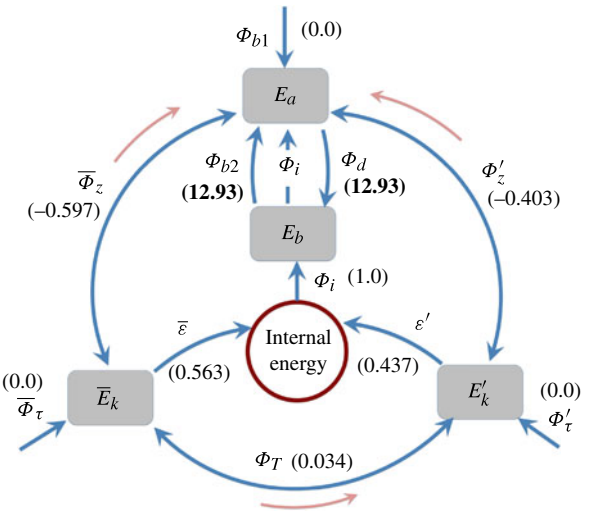


FIGURE 4. Schematic diagram showing the various forms and transformations of mechanical energy in a density-stratified flow of a linear Boussinesq fluid (Hughes *et al.* 2009). The forms of energy in a fixed volume of fluid are kinetic energy, E_k, available potential energy, E_a, background potential energy, E_b, and internal energy. External energy is supplied to the fluid by surface stresses at a rate Φ_τ and by net buoyancy input at any level at a rate Φ_{b1}. Energy is exchanged between the available potential and kinetic forms by the buoyancy fluxes, $\overline{\Phi}_z$ and Φ'_z, and between the mean and turbulent kinetic forms by the shear production Φ_T. Here $\overline{\varepsilon}$ and ε' are the rates of viscous dissipation from the kinetic energy reservoir. Transfers between the reservoirs of available and background potential energy include irreversible mixing, Φ_d, the release of internal energy by molecular diffusion (down the background gradient), Φ_i, and the differential buoyancy input at a given level, Φ_{b2}. Where energy transfers can be bidirectional, an additional arrow denotes the positive direction. In parentheses are the volume-integrated, time-averaged conversion rates (normalized by Φ_i) calculated in the present DNS with applied ΔT.

Region	$-\overline{\Phi}_z/\Phi_i$	$-\Phi'_z/\Phi_i$	$\overline{\varepsilon}/\Phi_i$	ε'/Φ_i	Φ_d/Φ_i
1 LBL	−235.78	0.28	0.43	0.28	**12.88**
2 Plume	**1840.91**	0.11	0.10	0.13	0.02
3 UBL	120.36	0.00	0.01	0.00	0.01
4 Interior	**−1724.89**	0.01	0.02	0.03	0.02
Box total	0.60	0.40	0.56	0.44	**12.93**

TABLE 1. Time-averaged contributions to mean buoyancy flux ($\overline{\Phi}_z$), buoyancy flux associated with the fluctuating flow component (Φ'_z), mean dissipation ($\overline{\varepsilon}$), turbulent dissipation (ε'), and irreversible mixing (Φ_d) in the different regions of the flow for applied ΔT, normalized by $\Phi_i = 5.5 \times 10^{10}(\rho_0\kappa^3/L)$. See figure 2(*a*) for regions. Box totals for the applied flux case are (in same order as the bottom line) 0.59, 0.41, 0.554, 0.446, 11.1, with $\Phi_i = 5.78 \times 10^{10}(\rho_0\kappa^3/L)$.

https://doi.org/10.1017/jfm.2012.592 Published online by Cambridge University Press

all terms in the global energy budget. Indeed, these rates of APE to KE conversion dominate the local energy budget. Similar results are found for applied boundary flux.

4. Scaling analysis

There is no net volume transport through any level and the net KE to APE conversion can be decomposed exactly (in a different manner from the boxes in figure 2*a*) as

$$\Phi_z = g\int_{V_+} \rho w \,\mathrm{d}V_+ + g\int_{V_-} \rho w \,\mathrm{d}V_- = g\int_{V_+} (\rho-\rho_a) w \,\mathrm{d}V_+ + g\int_{V_-} (\rho-\rho_a) w \,\mathrm{d}V_-. \quad (4.1)$$

Here ρ_a is an arbitrary constant and V could be arbitrarily divided into a number of sub-volumes, but we choose V_+ and V_- according to where $w>0$ and $w<0$, respectively. We now develop new scaling for horizontal convection (for applied ΔT), and proceed on the assumption that V_+ and V_- will approximately correspond to the plume and downwelling regions (V_2 and $V_{1,4}$, respectively; figure 2*a*). The flow can be characterized by estimating the contributions to Φ_z by writing (4.1) in the form

$$\Phi_z \approx -g\int_{V_2} \rho_0\alpha(T-\langle T\rangle_H) w \,\mathrm{d}V_2 - g\int_{V_{1+4}} \rho_0\alpha(T-\langle T\rangle_H) w \,\mathrm{d}V_{1+4} = I_+ + I_-. \quad (4.2)$$

Major contributions to the integrals in (4.2) arise from the boundary layer region of the flow. Both I_+ and I_- will have the same sign and can be estimated as

$$|I_+| \sim g\rho_0\alpha(T_h-\langle T\rangle_H)\psi_{bl} W\delta \quad \text{and} \quad |I_-| \sim g\rho_0\alpha(\langle T\rangle_H - T_c)\psi_{bl} W\delta/4, \quad (4.3)$$

where we assume that $\psi_{bl} = c_1\kappa Ra^{1/5}$ and $\delta = c_2 LRa^{-1/5}$ (Rossby 1965) for the volume transport (per unit width) and depth of the boundary layer, respectively, with c_1 and c_2 constants of $O(1)$ and the mean temperature in the boundary layer above the cold plate (area $WL/2$) is estimated as $0.5(\langle T\rangle_H + T_c)$. As $T_h - \langle T\rangle_H$ is considerably less than $\langle T\rangle_H - T_c$, we anticipate that I_- will make the dominant contribution to Φ_z; hence the centre of mass of the volume is not significantly affected by the density field in the plume. Thus $|I_-| \approx |\Phi_z|$, and as above $-\Phi_z = \varepsilon = \Phi_i$, which is consistent with $\Phi_i = g\kappa\rho_0\alpha(\langle T\rangle_H - \langle T\rangle_0)WL$ because $\langle T\rangle_0 = (T_c+T_h)/2$ and, at this level of approximation, $\langle T\rangle_H \approx T_h$.

Heating of the boundary layer fluid raises the centre of mass of the volume and also generates APE (figure 4). The rate at which the first of these effects occurs is estimated as the product of the change in potential energy per unit volume of fluid warmed in the boundary layer ($g\rho_0\alpha\Delta T\delta/2$) and the volume transport in the boundary layer ($\psi_{bl}W$). However, as there is no net change of potential energy in the volume, this effect is counteracted by a lowering of the centre of mass owing to cooling of the water drawn from the interior into the boundary layer above the cold base. This lowering occurs at a rate Φ_i ($\sim g\rho_0\alpha\Delta T\delta\psi_{bl}W/2$), which is a restatement of the result above ($|I_-| \sim \Phi_i$) from a physical perspective.

The rate of APE generation by the thermal forcing (i.e. Φ_{b2}) is dependent upon the height of the domain, and is estimated as the product of H and the buoyancy flux in to or out of the volume. A good estimate of the latter quantity is based on the conduction of heat through the boundary layer to the cold base, thus

$$\Phi_{b2} \approx g\rho_0\kappa\alpha\frac{(\langle T\rangle_H - T_c)}{\delta}\frac{WL}{2}H \sim \frac{\Phi_i}{2c_2}\left(\frac{\langle T\rangle_H - T_c}{\langle T\rangle_H - \langle T\rangle_0}\right) ARa^{1/5}. \quad (4.4)$$

https://doi.org/10.1017/jfm.2012.592 Published online by Cambridge University Press

The temperature differences $\langle T\rangle_H - T_c$ and $T_h - \langle T\rangle_H$ are determined by entrainment that couples the plume and interior, but may be related by noting that the release of APE by the plume above the height of the boundary layer is approximately 14 % of that supplied at the boundary (for a boundary layer whose depth $\delta_{0.95}$ accommodates 95 % of the temperature difference $\langle T\rangle_H - T_c$ (Hughes *et al.* 2007)). The rate of APE release by the plume is estimated as the product of the APE per unit volume of fluid entering the plume, $g\rho_0\alpha(T_h - \langle T\rangle_H)H$, and the volume transport in the boundary layer, $\psi_{bl}W$ (assuming $\delta/H \ll 1$). Thus, substituting (4.4) gives $(\langle T\rangle_H - T_c)/\Delta T = 1 - (T_h - \langle T\rangle_H)/\Delta T \approx 2c_1c_2/(0.14 + 2c_1c_2)$. Values of c_1 and c_2 are required for further progress: laboratory data, two-dimensional simulations and theory (Mullarney *et al.* 2004; Hughes *et al.* 2007) independently give $c_1 \approx 1.2$, 1.1 and 1.1, respectively, and $c_2 \approx 2.65$, 2.87 and 3.39, respectively, consistent with $c_1 = \psi_{bl}/(\kappa Ra^{1/5}) = 0.88$ and $c_2 = \delta_{0.95}Ra^{1/5}/L = 2.78$ from the current simulation. Using representative values, $c_1 = 1$ and $c_2 = 2.7$, we obtain $(\langle T\rangle_H - T_c)/\Delta T = 0.97$, which compares with the value 0.952 from the simulation (figure 2) and 0.92 derived from our experimental data. Furthermore, the above scaling estimates indicate $g\kappa\rho_0\alpha\Delta TWL/2\Phi_i$ $(\sim |I_-|/\Phi_i \approx |\Phi_z|/\Phi_i = \varepsilon/\Phi_i) \approx 1$ and, from (4.4), $\Phi_{b2}/\Phi_i \approx ARa^{1/5}c_2^{-1}\,(1 - 0.07/c_1c_2)^{-1}$. Note also that the Nusselt number $Nu \sim (\langle T\rangle_H - T_c)L/\Delta T\delta$, hence (4.4) gives $\Phi_{b2}/\Phi_i \sim ANu(0.07 + c_1c_2)/(0.07 - c_1c_2)$. For the conditions used in the DNS, $\Phi_{b2}/\Phi_i \approx 13.7$, which compares well with the computed value of 12.93 (figure 4).

Given $\Phi_{b2} = \Phi_d$, these energy conversions can be used to characterize horizontal convection in terms of a turbulent mixing efficiency, defined here as

$$\eta = (\Phi_d - \Phi_i)/(\Phi_d - \Phi_i + \varepsilon) = 1 - \Phi_i/\Phi_d. \tag{4.5}$$

Note that we avoid the definition $\eta = \Phi_d/(\Phi_d + \Phi_i)$ used by Scotti & White (2011), which is non-zero in a stationary stratified fluid when $\Phi_i = \Phi_d$. Thus (4.4) gives $1 - \eta \sim c_2(1 - 0.07/c_1c_2)A^{-1}Ra^{-1/5}$ $(\sim A^{-1}Nu^{-1}(0.07 - c_1c_2)/(0.07 + c_1c_2))$, which evaluates to $1 - \eta \sim 0.073$ for the values of A and Ra considered here. This scaling estimate compares well with the DNS value $1 - \eta = 0.077$ ($\eta = 92.3$ %), both indicating that horizontal convection is highly efficient in the sense that a strong overturning circulation and irreversible mixing occur with minimal viscous dissipation. A key point is that most of the buoyancy flux associated with the basal heating is absorbed in the convective mixed layer, from where we would expect the dominant contribution to Φ_d. In fact the DNS shows that 99.6 % of Φ_d is associated with the lower boundary layer (table 1), 93 % occurring adjacent to the heated boundary, where temperature gradients are unstable. The horizontal advection of cold fluid and vertical confinement of heating to the lower boundary layer allows local temperature gradients to be enhanced (relative to the gradients that would exist if vertical motion was uncapped). This results in remarkably efficient irreversible mixing compared with traditional mechanisms that involve turbulent stirring (and relatively high viscous dissipation) in a density stratification. This picture is consistent with the majority (71 %) of the viscous dissipation occurring in the lower boundary layer, where the flow length scales are small and three-dimensional flow structures are maintained (see figure 3) by fluctuating APE to KE conversion (Φ_z').

As viscous dissipation above the boundary layer is a minor term in the energy budget (table 1), the maximum overturning streamfunction ψ_{max} can be constrained using conservation of energy. Assuming the plume width $R \ll L$ at every level, conservation of volume can be used to show that, at levels beyond the boundary layer, the bulk of the kinetic energy in the mean flow is associated with the relatively

https://doi.org/10.1017/jfm.2012.592 Published online by Cambridge University Press

high velocity region in the plume. We expect the typical maximum flux of mean flow kinetic energy in the plume, $0.5\rho_0 W \max(\int_0^R \bar{u}_i^2 \bar{w}\,\mathrm{d}x) \sim 0.5\rho_0 W \psi_{max}^3/R_{max}^2$, to be limited by the conversion rate of residual APE above the boundary layer, $0.14\Phi_{b2}$. Substituting (4.4) gives

$$\psi_{max}/\psi_{bl} \lesssim 0.14^{1/3} c_1^{-2/3} (c_1 c_2 + 0.07)^{-1/3} (R_{max}/H)^{2/3} APr^{1/3} Ra^{1/5}. \tag{4.6}$$

We estimate the maximum plume width near the top as $R_{max} \approx \delta + 0.1H$, assuming it increases owing to entrainment (the half-angle of expansion being 0.1 (Turner 1986)) from an approximate width δ upon exiting the boundary layer, consistent with the DNS. Equation (4.6) predicts $\psi_{max}/\psi_{bl} \lesssim 7$, compared with a value of 2 from the simulation.

5. Conclusions

The computed temperature field and flow structure of horizontal convection shows good agreement with corresponding laboratory experiments, for both temperature and flux boundary conditions. The stably stratified boundary layer, formed above the cooled base, serves to trap small-scale instability and turbulent convection as the layer is drawn horizontally across the heated region. This maintains large density gradients in the convective mixed layer above the heated base, causes the mixed layer to be the site of almost all of the irreversible mixing that is required to balance the boundary buoyancy forcing (APE generation), and is the physical mechanism responsible for an overall turbulent mixing efficiency close to one.

The mechanical energy budget shows that, in this large-Rayleigh-number regime, horizontal convection is strongly dominated by available potential energy, which is generated by the thermal forcing and then released to kinetic energy – primarily in the base of the plume. The box-scale circulation gives rise to oppositely signed local buoyancy fluxes in the interior and plume that are individually several orders of magnitude larger than the net buoyancy flux in the flow. In terms of box-integrated quantities, the DNS confirms the theoretical prediction of a dominant and exact balance between boundary buoyancy forcing and irreversible mixing, mostly in the unstable boundary layer. A scaling analysis successfully predicts the magnitude of these quantities. These results explain why the convection is much stronger than might be inferred from previous emphasis on minor terms (the buoyancy flux–viscous dissipation balance, or the potential energy budget).

Although the simulated conditions are not far into the large-Rayleigh-number regime, it is not currently practicable to obtain DNS for still larger Ra. However, the energy scaling analysis predicts that, as Ra is increased, the magnitude of the circulation and the rates of available potential energy generation, irreversible mixing and viscous dissipation all increase. The rate of irreversible mixing has a stronger dependence upon Ra than does viscous dissipation and, consistent with the analysis of Scotti & White (2011), the mixing efficiency characterizing horizontal convection is expected to approach unity in the limit of infinite Rayleigh number.

Acknowledgements

Numerical computations were conducted using the Australian National Computational Infrastructure, ANU. This work was supported by Australian Research Council grants DP1094542 and DP120102744. G.O.H. was supported by ARC Future Fellowship FT100100869.

https://doi.org/10.1017/jfm.2012.592 Published online by Cambridge University Press

Supplementary movies

Supplementary movies are available at http://dx.doi.org/10.1017/jfm.2012.592.

References

GREGORY, J. M. & TAILLEUX, R. 2011 Kinetic energy analysis of the response of the Atlantic meridional overturning circulation to CO_2-forced climate change. *Clim. Dyn.* **37**, 893–914.

HUGHES, G. O. & GRIFFITHS, R. W. 2008 Horizontal convection. *Annu. Rev. Fluid Mech.* **40**, 185–208.

HUGHES, G. O., GRIFFITHS, R. W., MULLARNEY, J. C. & PETERSON, W. H. 2007 A theoretical model for horizontal convection at high Rayleigh number. *J. Fluid Mech.* **581**, 251–276.

HUGHES, G. O., HOGG, A. MCC. & GRIFFITHS, R. W. 2009 Available potential energy and irreversible mixing in the meridional overturning circulation. *J. Phys. Oceanogr.* **39**, 3130–3146.

MULLARNEY, J. C., GRIFFITHS, R. W. & HUGHES, G. O. 2004 Convection driven by differential heating at a horizontal boundary. *J. Fluid Mech.* **516**, 181–209.

PAPARELLA, F. & YOUNG, W. R. 2002 Horizontal convection is non-turbulent. *J. Fluid Mech.* **466**, 205–214.

ROSSBY, H. T. 1965 On thermal convection driven by non-uniform heating from below: an experimental study. *Deep Sea Res.* **12**, 9–16.

ROSSBY, H. T. 1998 Numerical experiments with a fluid heated non-uniformly from below. *Tellus* A **50**, 242–257.

SAENZ, J. A., HOGG, A. MCC., HUGHES, G. O. & GRIFFITHS, R. W. 2012 Mechanical power input from buoyancy and wind to the circulation in an ocean model. *Geophys. Res. Lett.* **39**, L13605.

SCOTTI, A. & WHITE, B. 2011 Is horizontal convection really "non-turbulent"? *Geophys. Res. Lett.* **38**, L21609.

STEVENS, R. J. A. M., VERZICCO, R. & LOHSE, D. 2010 Radial boundary layer structure and Nusselt number in Rayleigh–Bénard convection. *J. Fluid Mech.* **643**, 495–507.

STEWART, K. D., HUGHES, G. O. & GRIFFITHS, R. W. 2011 When do marginal seas and topographic sills modify the ocean density structure? *J. Geophys. Res.* **116**, C08021.

STEWART, K. D., HUGHES, G. O. & GRIFFITHS, R. W. 2012 The role of turbulent mixing in an overturning circulation maintained by surface buoyancy forcing. *J. Phys. Oceanogr.* **42**, 1907–1922.

TAILLEUX, R. 2009 On the energetics of stratified turbulent mixing, irreversible thermodynamics, Boussinesq models and the ocean heat engine controversy. *J. Fluid Mech.* **638**, 339–382.

TURNER, J. S. 1986 Turbulent entrainment: the development of the entrainment assumption, and its application in geophysical flows. *J. Fluid Mech.* **173**, 431–471.

WINTERS, K. B., LOMBARD, P. N., RILEY, J. J. & D'ASARO, E. A. 1995 Available potential energy and mixing in density-stratified fluids. *J. Fluid Mech.* **289**, 115–128.

https://doi.org/10.1017/jfm.2012.592 Published online by Cambridge University Press